Grating-assisted fabrication of sub-wavelength ripples during femtosecond laser processing of dielectrics

Yanping Yuan (袁艳萍)* and Jimin Chen (陈继民)

Institute of Laser Engineering, Beijing University of Technology, Beijing 100124, China
**Corresponding author: ypyuan@bjut.edu.cn*

Received September 30, 2015; accepted November 6, 2015; posted online December 17, 2015

During the formation of sub-wavelength ripples, the initial surface plasmon (SP)-laser interference plays an important role. In this Letter, the effects of grating structures on the distribution of the absorbed laser intensity, SP-laser coupling, free electron distributions, and ablation shapes are investigated by the plasma model, taking into consideration both the laser wave-particle duality and the transient localized changes of material properties. The simulation results show that the grating structures can strongly enhance the energy absorption and SP-laser coupling, which makes the fabrication of sub-wavelength ripples more efficient. It is also found that the ablation shapes, in terms of ablation depths and sub-wavelength ripples periods, are strongly related to the grating structures, which can be used to control micro/nanostructures precisely and uniformly.

OCIS codes: 140.3390, 220.4241, 320.7090.
doi: 10.3788/COL201614.011404.

A femtosecond laser pulse in some aspects fundamentally changes the laser-material interaction mechanisms as compared with a long pulse. Femtosecond lasers are currently becoming very common tools for laser materials processing, both in fundamental investigations and for various applications such as optical waveguides[1,2], microfluidic devices[3,4], and bioscaffolds[5]. Laser-induced periodic surface structures (LIPSS/ripples) can be observed on various materials and are almost a universal phenomenon[6–10], which is of great interest for various applications[11,12]. Ripples with periods close to the wavelengths of the incident lasers are caused by the interference between the incident laser waves and the surface scattered waves[13,14]. Also, sub-wavelength ripples with periods significantly smaller than the incident laser wavelengths are reported. Lots of processing parameters affect the formation of sub-wavelength ripples strongly, including the central wavelength[15], incidence angle[16], pulse number[17], laser fluence[18–20], polarization[21], pulse delay[22], and processing environments[23–25]. The interference between the incident laser and the laser-induced surface electromagnetic wave is the most widely accepted explanation of sub-wavelength ripples formation[26,27]. There are also some other hypotheses to explain the phenomenon, e.g., self-organization[28,29], second harmonic generation[30], and the Coulomb explosion[31]. As mentioned above, one crucial parameter for sub-wavelength formation is the pulse number[32–36], due to the strong effects of initial grating structures on surface plasmon (SP)-laser coupling[27,37–40]. However, it remains a significant challenge to effectively control sub-wavelength ripples fabrication, which requires a new theoretical and experimental understanding.

In this Letter, a plasma model that considers both the laser wave-particle duality and transient localized changes of material properties is employed to investigate the interaction between the laser and fused silica. The focus of this study is the effects of grating structures on the distribution of the absorbed laser intensity, SP-laser coupling, free electron distributions, and ablation shapes. It is found that the grating structures strongly enhance SP-laser coupling, which makes the fabrication of sub-wavelength ripples more efficient. The ablation shapes (including periods of sub-wavelength ripples and ablation depths) can be manipulated by designing the grating structures, which can be used to control micro/nanostructures precisely and uniformly.

In the proposed model, it is assumed that the incident laser with the transverse magnetic field propagates along the z-axis:

$$\vec{H}_i(t,r,z) = H_0 \exp\left(-2\ln 2\frac{t^2}{t_p^2} - \frac{r^2}{r_0^2}\right)\exp(-\boldsymbol{\alpha}(t,r,z)z) \times \exp(i(k_r r + k_z z) - iwt), \quad (1)$$

where H_0 and $H_i(t,r,z)$ are the peak incident magnetic field and the envelope of the incident magnetic field, respectively. For a given amplitude $\boldsymbol{H_i}(t,r,z)$ of the magnetic vector, t represents the time, r represents the distance to the Gaussian beam axis, and z represents the depth from the surface of the bulk material. t_p represents the pulse duration, r_0 represents the radius of the laser beam, k_r represents the wave number along the r-axis, k_z represents the wave number along the z-axis, and the laser center frequency is represented by $\boldsymbol{\omega}$.

At the interface between a dielectric with a permittivity ε_D and the air with a permittivity ε_A, if the value of the real component of the complex dielectric function is less than -1, the SPs can be resonantly excited by the coupling between the surface electrons of the dielectric and the incident field, which is characterized by surface electromagnetic waves. The distribution of each component A of the electric and magnetic fields at frequency

ω in a plane surface electromagnetic wave traveling along the r-axis has the form[26] of $A(t,r,z) = A_0 \exp(i\omega t - k_s r)$. The coupling field is the superposition of the incident field and the SP field, as detailed in Ref. [26].

It is assumed that the laser focus point is at the surface of the material, $z = 0$. At surface, the partially reflected laser beam is $I(t,r,0) = 2F/(\sqrt{\pi/\ln 2}t_p)(1 - R(t,r))$, where F is the laser (peak) fluence. The laser intensity inside of the bulk materials is expressed as

$$I(t,r,z) = |\vec{E}(t,r,z) \times \vec{H}(t,r,z)|. \quad (2)$$

The free electron generation[22,26] is calculated by the following equation:

$$\frac{\partial n_e(t,r,z)}{\partial t} = \alpha_i I(t,r,z) n_e(t,r,z) + \delta_N (I(t,r,z))^N - \frac{n_e(t,r,z)}{\tau}, \quad (3)$$

where $n_e(t,r,z)$ is the free electron density, τ is the free electron recombination time, α_i is the impact ionization constant, and δ_N is the cross section of N photon absorption. The Drude model is used to determine the optical properties of the ionized dielectrics. The absorption coefficient and the reflectivity on the surface can be determined by the Fresnel expression, as detailed in Ref. [26]. During the laser pulse duration, the lattice temperature in K (T_l) is assumed to be a constant (300 K), and the electron temperature (T_e) is determined by[22,26]

$$C_e(T_e, n_e) n_e(t,r,z) \frac{\partial T_e(t,r,z)}{\partial t} = \alpha_h(t,r,z) I(t,r,z), \quad (4)$$

where C_e is the specific heat of free electrons.

The numerical procedure in this study is as follows. The spatial and temporal dependents of the free electron densities, optical properties, thermal properties, and free electron temperatures are calculated using the following iterative scheme: (a) by considering the incident laser as electromagnetic waves, the distribution of the laser intensity is calculated by solving Eq. (2), (b) by considering the electrons/plasma of the materials as particles, the distribution of the electron densities is calculated by solving Eq. (3), (c) the distribution of the electron temperature is calculated by solving Eq. (4), (d) the spatial and temporal dependence of the optical properties and thermal properties are then updated, and (e) in the next time step, the iterative scheme is continued until the end of the pulse duration.

Using the plasma model that considers both the laser wave-particle duality and the transient localized changes of material properties, we investigate the effects of grating structures on the distribution of the absorbed laser intensity, SP-laser coupling, free electron distributions, and ablation shapes. This study calculates a linearly polarized laser pulse train (the wavelength of 800 nm, the pulse duration of 50 fs) ablation of fused silica. Laser pulse trains are considered as a train with two pulses with a separation time of 50 fs at a fluence of 4.0 J/cm^2. The rectangle wave-grating structures fabricated on the surface are described by three structural parameters, w, h, and d, which denote the width, depth, and period of the grating, respectively. The schematic diagram of the grating structure is as shown in Fig. 1.

Based on our previous study[22,26], free electrons are gradually generated by photoionization and impact ionization during the interaction between the laser and fused silica. With the increase of the free electrons, the optical properties and thermal properties of the materials are significantly changed, leading to changes in the intensity distributions. Figure 2 shows the spatial distributions of the incident intensities at 120 fs and different grating constants: (a) flat structure (grating constant $w = 0$ nm, $d = 0$ nm, $h = 0$ nm), (b) grating constant $w = 50$ nm, $d = 100$ nm, $h = 10$ nm, (c) grating constant $w = 50$ nm, $d = 120$ nm, $h = 10$ nm, and (d) grating constant $w = 70$ nm, $d = 120$ nm, $h = 10$ nm. As shown in Fig. 2(a), the incident intensity in the central area is strongly reshaped due to the strong reflectivity from the surface. After reflection, the distribution of the absorbed laser field occurs with spatially periodic patterns in the central area. As compared with the case in Fig. 2(a),

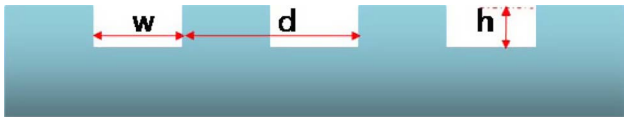

Fig. 1. Schematic diagram of grating structure.

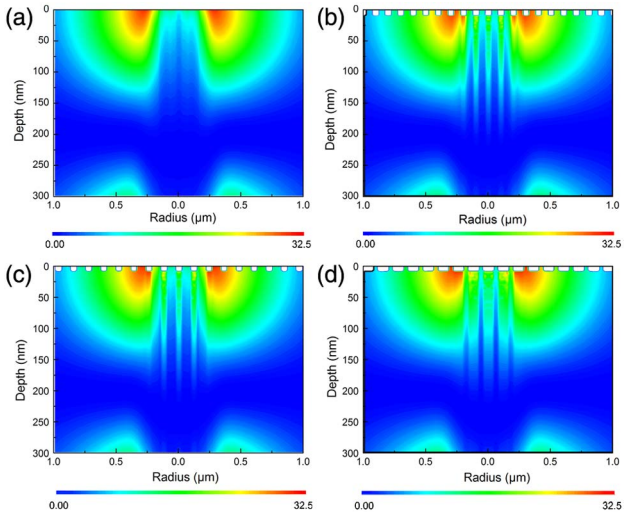

Fig. 2. Spatial distributions of incident intensities at 120 fs and different grating constants: (a) flat structure ($w = 0$ nm, $d = 0$ nm, $h = 0$ nm), (b) grating constant $w = 50$ nm, $d = 100$ nm, $h = 10$ nm, (c) grating constant $w = 50$ nm, $d = 120$ nm, $h = 10$ nm, and (d) grating constant $w = 70$ nm, $d = 120$ nm, $h = 10$ nm.

the grating-assisted absorption is obviously enhanced, which makes the spatial periodic patterns of the intensity distribution clearer. As shown in Figs. 2(b)–2(d), the enhanced laser intensity is mainly localized in the grooves. The simulation result shows that periods of patterns are different at various grating constants, which are in agreement with the periods of the grating structures. Hence, the absorbed laser field can be adjusted by designing the structures of the gratings.

During the formation of sub-wavelength ripples, the interference between the SPs and the incident laser plays an important role[26]. Figure 3 shows spatial distributions of SP-laser coupling intensities at 120 fs and different grating constants: (a) flat structure, (b) grating constant $w = 50$ nm, $d = 100$ nm, $h = 10$ nm, (c) grating constant $w = 50$ nm, $d = 120$ nm, $h = 10$ nm, and (d) grating constant $w = 70$ nm, $d = 120$ nm, $h = 10$ nm. As shown in Figs. 3(b)–3(d), it is easily found that the grating structures can significantly enhance the SP-laser coupling, and the SP-laser coupling intensities are much more intense in the grooves, which is in agreement with the simulation results in Ref. [39]. The simulation results also show that grating-assisted SP-laser coupling makes the spatial periodic pattern of the coupling intensity more uniform.

Based on our previous study[26], the spatial periodic pattern of the coupling intensity leads to the periodic distribution of free electrons and surface structures. According to our assumption[26], if the densities of free electrons are greater than the critical density, the ablation has started. As shown in Fig. 4, the lines trace the locations with the critical density, and the crater curve marks the boundaries at which the critical electron density is reached. As shown in Fig. 4, it is easily found that the grating constants strongly affect the morphologies of the surface structures.

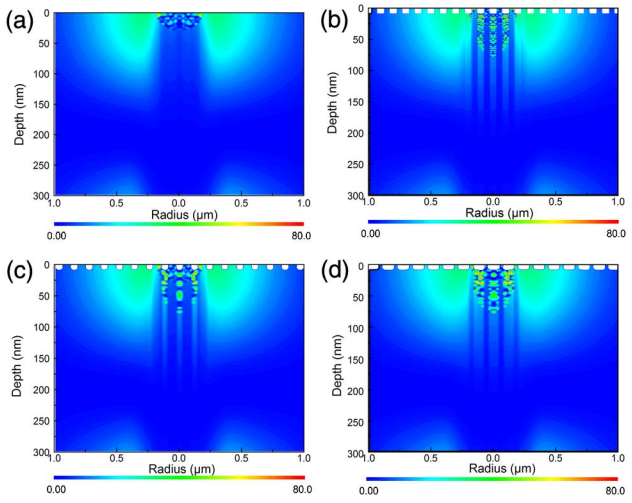

Fig. 3. Spatial distributions of SP-laser coupling intensities at 120 fs and different grating constants: (a) flat structure, (b) grating constant $w = 50$ nm, $d = 100$ nm, $h = 10$ nm, (c) grating constant $w = 50$ nm, $d = 120$ nm, $h = 10$ nm, and (d) grating constant $w = 70$ nm, $d = 120$ nm, $h = 10$ nm.

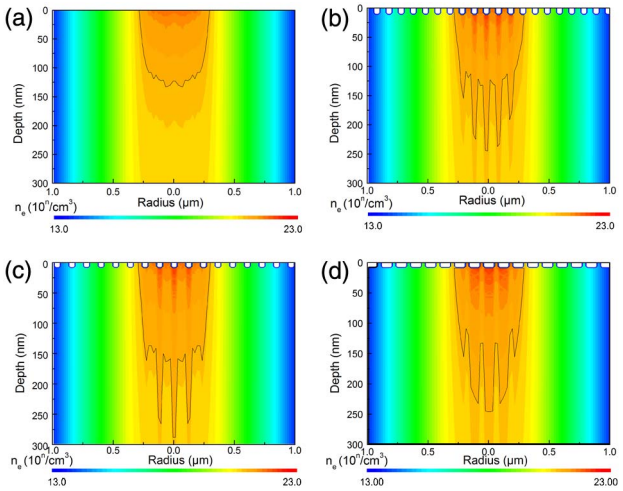

Fig. 4. Spatial distributions of free electron density and ablation shapes at the end of laser pulse train irradiation and different grating constants: (a) flat structure, (b) grating constant $w = 50$ nm, $d = 100$ nm, $h = 10$ nm, (c) grating constant $w = 50$ nm, $d = 120$ nm, $h = 10$ nm, and (d) grating constant $w = 70$ nm, $d = 120$ nm, $h = 10$ nm.

The simulation results show that the radii of the ablation craters are independent of the grating structures. The radius of the ablation crater is 290 nm. The ablation depths and the periods of sub-wavelength ripples are strongly affected by the grating structures, as shown in Fig. 4. As in the flat structure case shown in Fig. 4(a), the maximum ablation depth is 138 nm, and the period of the sub-wavelength ripple is about 80 nm. As shown in Fig. 4(b), the maximum ablation depth is 250 nm, and the period of sub-wavelength ripple is about 100 nm. The period of the sub-wavelength ripple (about 120 nm) in Fig. 4(c) is the same as that in Fig. 4(d). As shown in Fig. 2, the field intensity is localized in the grooves, which leads to the enhancement of SP-laser coupling in the grooves. Hence, more free electrons can be generated in the grooves than in the ridges between the grooves, which causes the dependence between the period of the sub-wavelength ripple and the grating structures. However, the maximum ablation depths are different. For the case of the grating constant with $w = 50$ nm and $d = 120$ nm, the maximum ablation depth is 280 nm. As shown in Fig. 4(d), the maximum ablation depth is 250 nm. The simulation results show that the control of the sub-wavelength ripples can be conducted by designing grating structures. It can be used to adjust micro/nanostructures precisely, uniformly, and efficiently.

In conclusion, the periods of sub-wavelength ripples are mainly determined by the interference between the SPs and the incident laser during the femtosecond laser pulse trains processing of fused silica. The initial SP-laser coupling plays an important role during the formation of sub-wavelength ripples. This Letter investigates the effects of grating structures on the distribution of the absorbed laser intensity, SP-laser coupling, and the ablation shapes by a plasma model that considers both the laser wave-particle

duality and the transient localized changes of material properties. The simulation results show that the grating structures strongly enhance the absorbed laser intensity and SP-laser coupling and make them concentrate on the grooves. The uniform periodic patterns of energy in agreement with the grating structures make the sub-wavelength ripples depend on the grating parameters, which makes the fabrication of the sub-wavelength ripple more efficient.

This work was financially supported by the Municipal Science and Technology Project (Nos. Z141100002814011 and Z141100002814011), the Beijing National Basic Research Program of China (No. 2011CB013000), and the China Postdoctoral Science Foundation.

References

1. G. Della Valle, R. Osellame, and P. Laporta, J. Opt. A: Pure Appl. Opt. **11**, 013001 (2009).
2. M. Ams, P. Dekker, G. D. Marshall, and M. J. Withford, Opt. Lett. **37**, 993 (2012).
3. K. Sugioka and Y. Cheng, *Femtosecond laser 3D micromachining for microfluidic and optofluidic applications* (Springer, 2013).
4. D. Wu, Q. Chen, L. Niu, J. Wang, J. Wang, R. Wang, H. Xia, and H. Sun, Lab. Chip **9**, 2391 (2009).
5. S. Rekštyté, M. Malinauskas, and S. Juodkazis, Opt. Express **21**, 17028 (2013).
6. F. Meng, J. Hu, W. Han, P. Liu, and Q. Wang, Chin. Opt. Lett. **13**, 062201 (2015).
7. Z. Cui, Y. Li, W. Wang, C. Lin, and B. Xu, Chin. Opt. Lett. **13**, 011402 (2015).
8. X. Shi, L. Jiang, X. Li, K. Zhang, D. Yu, Y. Yu, and Y. Lu, J. Appl. Phys. **116**, 033104 (2014).
9. X. Jia, Y. Yuan, D. Yang, T. Jia, and Z. Sun, Chin. Opt. Lett. **12**, 113203 (2014).
10. P. Feng, L. Jiang, X. Li, W. Rong, K. Zhang, and Q. Cao, Appl. Opt. **54**, 1314 (2015).
11. B. Dusser, Z. Sagan, H. Soder, N. Faure, J. P. Colombier, M. Jourlin, and E. Audouard, Opt. Express **18**, 2913 (2010).
12. A. Y. Vorobyev and C. Guo, Appl. Phys. Lett. **92**, 041914 (2008).
13. D. C. Emmony, R. P. Howson, and L. J. Willis, Appl. Phys. Lett. **23**, 598 (1973).
14. J. E. Sipe, J. F. Young, J. S. Preston, and H. M. van Driel, Phys. Rev. B **27**, 1141 (1983).
15. C. Albu, A. Dinescu, M. Filipescu, M. Ulmeanu, and M. Zamfirescu, Appl. Surf. Sci. **278**, 347 (2013).
16. Q. Wu, Y. Ma, R. Fang, Y. Liao, Q. Yu, X. Chen, and K. Wang, Appl. Phys. Lett. **82**, 1703 (2003).
17. J. Bonse and J. Krüger, J. Appl. Phys. **108**, 034903 (2010).
18. Y. P. Yuan, J. M. Chen, and F. R. Liu, Adv. Mater. Res. **1035**, 426 (2014).
19. Y. Li, F. Liu, Y. F. Li, L. Chai, Q. R. Xing, M. L. Hu, and C. Y. Wang, Appl. Opt. **50**, 1958 (2011).
20. F. Liang, R. Vallée, and S. L. Chin, Appl. Phys. Lett. **100**, 251105 (2012).
21. P. J. Liu, L. Jiang, J. Hu, W. N. Han, and Y. F. Lu, Opt. Lett. **38**, 1969 (2013).
22. Y. P. Yuan, L. Jiang, X. Li, C. Wang, and Y. Lu, J. Appl. Phys. **112**, 103103 (2012).
23. M. Y. Shen, J. E. Carey, C. H. Crouch, M. Kandyla, H. A. Stone, and E. Mazur, Nano Lett. **8**, 2087 (2008).
24. M. Ulmeanu, F. Jipa, C. Radu, M. Enculescu, and M. Zamfirescu, Appl. Surf. Sci. **258**, 9314 (2012).
25. G. L. Deng, G. Y. Feng, K. Liu, and S. H. Zhou, Appl. Opt. **53**, 3004 (2014).
26. Y. P. Yuan, L. Jiang, X. Li, C. Wang, H. Xiao, Y. Lu, and H. Tsai, J. Phys. D **45**, 175301 (2012).
27. M. Huang, F. L. Zhao, Y. Cheng, N. Xu, and Z. Z. Xu, ACS Nano **3**, 4062 (2009).
28. J. Reif, O. Varlamova, S. Varlamov, and M. Bestehorn, Appl. Phys. A **104**, 969 (2011).
29. J. Reif, O. Varlamova, and F. Costache, Appl. Phys. A **92**, 1019 (2008).
30. R. Le Harzic, D. Dörr, D. Sauer, M. Neumeier, M. Epple, H. Zimmermann, and F. Stracke, Opt. Lett. **36**, 229 (2011).
31. Y. Dong and P. Molian, Appl. Phys. Lett. **84**, 10 (2004).
32. F. Liang, R. Vallée, and S. L. Chin, Opt. Express **20**, 4389 (2012).
33. W. Zhang, G. Cheng, and Q. Feng, Appl. Surf. Sci. **263**, 436 (2012).
34. S. Höhm, A. Rosenfeld, J. Krüger, and J. Bonse, J. Appl. Phys. **112**, 014901 (2012).
35. J. Bonse, S. Höhm, A. Rosenfeld, and J. Krüger, Appl. Phys. A **110**, 547 (2013).
36. T. T. Dai Huynh, A. Petit, and N. Semmar, Appl. Surf. Sci. **302**, 109 (2014).
37. R. D. Murphy, B. Torralv, D. P. Adams, and S. M. Yalisove, Appl. Phys. Lett. **103**, 141104 (2013).
38. X. Jia, T. Q. Jia, N. N. Peng, D. H. Feng, S. A. Zhang, and Z. R. Sun, J. Appl. Phys. **115**, 143102 (2014).
39. J. W. Yao, C. Y. Zhang, H. Y. Liu, Q. F. Dai, L. J. Wu, S. Lan, A. V. Gopal, V. A. Trofimov, and T. M. Lysak, Opt. Express **20**, 905 (2012).
40. M. Huang, Y. Cheng, F. Zhao, and Z. Xu, Ann. Phys. (Berlin) **525**, 74 (2013).